AIAA SciTech Forum
8-12 January 2024, Orlando, FL
AIAA SCITECH 2024 Forum

10.2514/6.2024-0688

Uncertainty and Data Analysis of ExB Probe including Field Non-Uniformity and Transmittancy

Toyofumi Yamauchi* and Joshua L. Rovey†
University of Illinois at Urbana-Champaign, Urbana, IL, 61801

An ExB probe is a pass-band velocity filter for an ion beam, and it can provide a measurement of the ion velocity distribution function (IVDF). However, the finite pass-band filter window size leads to differences in the true IVDF and measured ExB probe spectrum. The ExB probe spectra from three different ExB probe designs are compared to a synthetically defined test IVDF to study how the ExB probe geometry affects the differences. The E- and B-fields in the ExB probe is typically not uniform and not identical in shape, and this also leads to the difference in the IVDF and the ExB probe spectrum. An analytical formula that corrects the field non-uniformity effect is proposed in this work and is tested through the simulation of the single ion particle trajectory. The analytical correction formula captures the ion deflections under the non-uniform fields with an error of -1.0 mm (approximately 30% percentage difference) or less for the displacement and -750 m/s (approximately 33% percentage difference) or less for the velocity change. It is found that using the B-field strength at the center of the filter section overestimates the overall B-field strength and causes underestimation of the ion velocity by approximately 10%. In the second numerical experiment test, the two distinct, closely adjacent peaks, which are observable in one ExB probe design, become one large peak when the collimator and the drift tube lengths are halved from 130 mm to 65 mm. The ExB probe broadens the peak width up to 287%, in which case inferring the ion velocity spread from the ExB probe may not be a valid approach. The relative ion species fraction calculated from the ExB probe spectra showed a good agreement within an error of 0.1% or less. Finally, an approach to account for the space-charge ion beam expansion, which is often neglected in the ExB probe analysis is discussed.

I. Nomenclature

A_i	=	the cross-sectional area of aperture i, m^2
$B_x(z)$	=	the B-field strength profile in the x-direction along the z-direction, Tesla
$B_{x,0}$	=	the B-field strength in the x-direction at the center of the filter section, Tesla
$B_{x,i}$	=	the B-field strength in the x-direction at the i-th discretized section, Tesla
$B_{x,\text{eff}}$	=	the effective B-field strength in the x-direction, Tesla
$B_{x,\text{pra}}$	=	the practical B-field strength in the x-direction, Tesla
d_e	=	the distance between two electrodes, m
$E_y(z)$	=	the E-field strength profile in the y-direction along the z-direction, V/m
$E_{y,0}$	=	the E-field strength in the y-direction at the center of the filter section, V/m
$E_{y,i}$	=	the E-field strength in the y-direction at the i-th discretized section, V/m
$E_{y,\text{eff}}$	=	the effective electric field strength in the y-direction, V/m
f_k	=	the density fraction for ion k at the given velocity v, -
$\boldsymbol{f_k}$	=	the ion velocity distribution function, -
F_k	=	the amplitude of the peak for ion k in the test IVDF, -
$\boldsymbol{g_k}$	=	the ExB probe spectrum, -
$h(\alpha_x, \alpha_y)$	=	the probability of ion incident angles, -
$I_{c,k}$	=	the collected current for ion k, A
I_k	=	the current for ion k, A

*Graduate Research Assistant, Aerospace Engineering, 104 S. Wright St. Urbana, IL 61801, and AIAA Student Member. ty20@illinois.edu.
†Professor, Aerospace Engineering, 104 S. Wright St. Urbana, IL 61801, and AIAA Associate Fellow. rovey@illinois.edu.

$I_{peak,k}$ = the peak current for ion k, A
J_k = the current density for ion k, A/m^2
J_{tot} = the total ion current density at the inlet of the ExB probe, A/m^2
l_c = the length of the collimator section, m
l_d = the length of the drift tube section, m
l_f = the length of the filter section, m
m_k = the mass of ion k, kg
n_k = the number density of ion k, m^{-3}
N_α = the number of incident angles considered for $\overline{\boldsymbol{T}}_k$, -
N_s = the number of the discretized sections for the non-uniform E- and B-fields = $l_f/\delta z$, -
q_k = the charge of ion k, C
r_i = the radius of aperture i, m
r_o = the radius of orifice, m
V_{accel} = the ion acceleration potential, V
V_{plates} = the potential difference between two electrodes, V
v_k = the velocity of ion k, m/s
$\bar{v}_k$ = the average velocity of ion k, m/s
$v_{y,0}$ = the initial ion velocity in the y-direction = $v_k \sin(\alpha_y)$, m/s
v_z = the ion velocity in the z-direction, m/s
v_w = the Wien velocity, m/s
v_w^* = the corrected Wien velocity, m/s
S = the intersection area of four aperture circles, m^2
T_k = the transmittancy for ion k, -
$\boldsymbol{T_k}$ = the transmittancy matrix for ion $k \in [0, 1]$, -
$\overline{\boldsymbol{T}}_{\boldsymbol{k}}$ = the angular-averaged transmittancy matrix for ion k, -
α_{max} = the maximum ion incident angle, degree
α_x = the ion incident angle in the x-direction, degree
α_y = the ion incident angle in the y-direction, degree
δz = the length of the discretized section for the non-uniform E- and B-fields, m
Δv_w = the maximum deviation for the Wien velocity, m/s
Δx_c = the displacement of the ion beam in the x-direction at the collimator section, m
Δx_d = the displacement of the ion beam in the x-direction at the drift tube section, m
Δx_f = the displacement of the ion beam in the x-direction at the filter section, m
Δy_c = the displacement of the ion beam in the y-direction at the collimator section, m
Δy_d = the displacement of the ion beam in the y-direction at the drift tube section, m
$\Delta \tilde{y}_d$ = the corrected displacement of the ion beam in the y-direction at the drift tube section, m
Δy_f = the displacement of the ion beam in the y-direction at the filter section, m
$\Delta \tilde{y}_f$ = the corrected displacement of the ion beam in the y-direction at the filter section, m
μ_k = the peak velocity of ion k in the test IVDF, m/s
$\%_{n,k}$ = a relative fraction of number density for ion k, -
σ_k = the peak width or the standard deviation of ion k in the test IVDF, m/s

II. Introduction

AN ExB probe, also called a Wien filter, is a measurement device that selectively filters ions based on their velocity. An ExB probe is often used to estimate the energy state and the relative species fraction of ions during electric propulsion (EP) testing. When ions are accelerated by the same acceleration potential and gain the same kinetic energy, which is approximately true for many EP thrusters, the velocity of the ion can be estimated to be

$$v_{ion} = \sqrt{\frac{2q_k V_{accel}}{m_k}} \tag{1}$$

Unlike other diagnostic devices that measure the energy of ions, such as a retarding potential analyzer (RPA) or an electrostatic analyzer (ESA), the ExB probe can discern ions with different mass-to-charge (m/q) ratios. EP thrusters

operating with single gas propellant, such as xenon, typically produce an ion beam containing ions with different mass-to-charge ratios (e.g., Xe^{+}, Xe^{2+}, and Xe^{3+} from Xe propellant), and such multiply-charged ions affect a thruster's performance and erosion mechanism. ExB probes have been used in ion beam diagnostic testing for various EP thrusters, such as gridded ion engines (GIEs) [1–4] and Hall effect thrusters (HETs) [5–17], and even for the charged particles in a nozzle beamed flame [18]. Recently, there has been increased trend that replaces a traditional noble-gas propellant with an alternative molecular-based gas propellant. Since molecular-based gas propellants often produce ions with slightly different mass-to-charge ratios, the need to determine the energy state and the relative fraction of such ions is growing. The ExB probe is suitable for that purpose, and it has been used for discerning different ions in the alternative propellant EP ion beam, such as C_{60}^{+} and C_{60}^{-} in fullerene ion beam [19–23], SF_6-based ions in PEGASES project [24–27], and atmospheric species from the HET operating with Xe-air mixture [28, 29].

An ExB probe typically sweeps the filter velocity to obtain the ion velocity distribution function (IVDF). In fact, several ion parameters, such as the peak and average ion velocity, the ion energy spread, the structure of the ion acceleration region, and the relative ion species fraction, are inferred from the measured IVDF. However, it has been known that the shape of the measured I-V curve (i.e., ExB probe spectrum) is not same as the shape of the true IVDF due to the finite pass-band filter window size [14, 30]. To date, few studies have theoretically investigated how an ExB probe of a given geometry collects an IVDF as an ExB probe spectrum and how the difference between the true IVDF and the measured ExB probe spectrum propagates into the ion parameter calculations [16, 29]. There are currently no standard ExB probe design criteria. It is unclear how each ExB probe's geometric parameter relates to the difference between the true IVDF and the measured ExB probe spectrum.

The purpose of this work is to examine the ExB probe mechanism that causes the difference between the true IVDF and measured ExB probe spectrum. The fundamental ExB probe operating mechanism, the ExB probe spectrum collection mechanism, the E- and B-fields non-uniformity analysis, and the ion parameters that are based on the IVDF are explained in Sec. III.A, III.B, III.C and III.D, respectively. We conduct two numerical experiments in this work. In Section IV, the analytical formula correcting the field non-uniformity effect that is proposed in Sec. III.C is tested by the simulation of the single ion particle trajectory under the E- and B-fields. In Section V, the ExB probe spectrum is calculated from the given ExB probe geometry and the synthetically defined test IVDF by using the theory developed in Sec. III.B. Three ExB probe designs are tested to study how an ExB probe design affects the difference in the true IVDF and the measured ExB probe spectrum. Section VI discusses the approach that potentially reduces one of the assumptions used in this work. Finally, Section VII summarizes the findings of this work obtained through the numerical experiment tests.

III. Theory

A. ExB probe operating mechanism

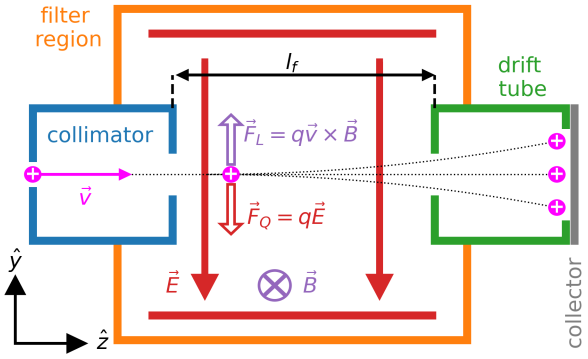

Fig. 1 The operation principle of a three-section ExB probe. The slightly deflected ions are still collected by the collector.

Figure 1 shows the operating mechanism of the ExB probe as a velocity filter. The electric field ($\vec{E}$) points in the

negative y-direction (downward), and the magnetic field ($\vec{B}$) points in the positive x-direction (into the page). When an ion k enters the filter section with a velocity $\vec{v} = v_k$, the ion experiences the electrostatic force ($\vec{F}_Q = q_k\vec{E}$) and the Lorentz force ($\vec{F}_L = q_k\vec{v} \times \vec{B}$). The ion continues the motion in a straight line and passes through the filter section when these two forces are equal and cancel each other ($\vec{F}_Q = \vec{F}_L$). When one force is stronger than another, the ion drifts in either the positive or negative y-direction and is filtered out by the applied ExB fields. For the given field strength, the velocity such that the two forces are equal is called the Wien velocity and is given by

$$v_w = \frac{E_y}{B_x} = \frac{V_{plates}}{B_x d_e} \tag{2}$$

B. ExB probe spectrum

1. Transmittancy

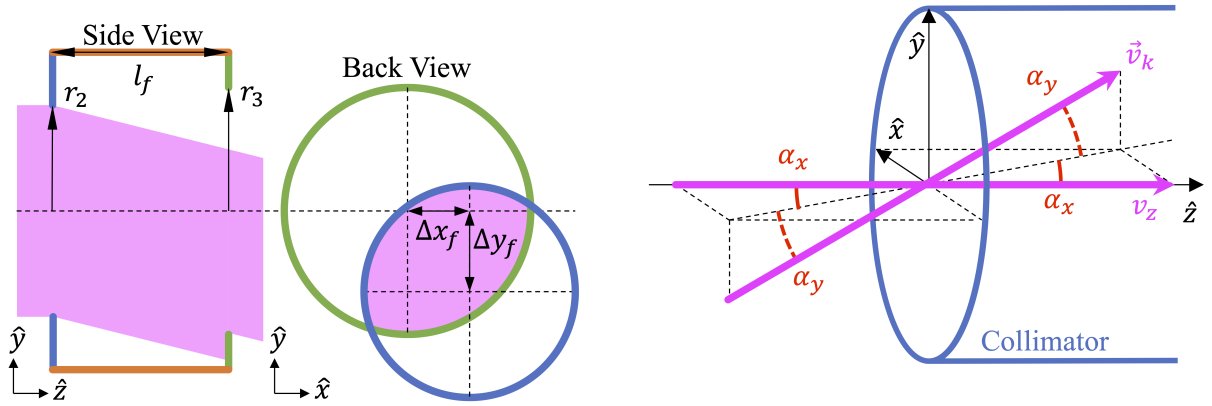

(a) The concept of transmittancy (represented as the intersection of two circles at the ExB region.) The ion beam is deflected in the x-axis by Δx_f and in the y-direction by $-\Delta y_f$ in this diagram.

(b) The ion entering the ExB probe with a velocity $\vec{v}_k$, an incident angle in the x-direction α_x, and an incident angle in the y-direction α_y. The velocity in the z-direction v_z can be expressed with Eq. 3.

Fig. 2 The diagrams for the transmittancy.

The transmittancy is the fraction of the incoming ions that transmits through the ExB probe in terms of collection area fraction, as illustrated in Fig. 2a. When all of the ions are collected, the transmittancy is 1. When none of the ions are collected, the transmittancy is 0. To analytically obtain the transmittancy, we calculate the ion beam trajectory based on the equation of motion [29], and we make the following assumptions:

1) Ions are not magnetized before entering the ExB probe and enter with a straight trajectory.
2) The space-charge effect and the collision between the incoming ions and the internal neutrals are negligibly small, and the ion beam does not diverge or converge in the ExB probe.
3) Electrons do not affect the ExB probe operation.
4) The flying angle of ions ($\alpha = \tan^{-1}\left(v_{x,y}/v_z\right)$) is small throughout the ExB probe, and the velocity in the z-direction is approximately the same as the ion speed ($v_z \approx v_k$).
5) The E- and B-fields are uniform and span over the filter region.
6) Negligible fields exist in the collimator and the drift tube sections.
7) E-field has no components in the x- and z-direction ($\vec{E} = E_y\hat{y}$).
8) B-field has no components in the y- and z-direction ($\vec{B} = B_x\hat{x}$).
9) An entrance aperture radius is equal to or smaller than an exit aperture radius at each section ($r_1 \leq r_2 \leq r_3 \leq r_4$).

Figure 2b describes the condition of the ion entering the ExB probe with a velocity $\vec{v}_k = v_x\hat{x} + v_y\hat{y} + v_z\hat{z}$. At the inlet of the ExB probe, the ion k may enter with initial incident angles in the x- and y-directions. The velocity in the z-direction can be represented as

$$v_z = v_k \cos\left(\alpha_x\right) \cos\left(\alpha_y\right) \tag{3}$$

While traveling along the z-axis of the ExB probe with a velocity of v_z, the ion k also moves in the x- and y-directions due to the ExB fields and due to the initial velocity in the x- and y-directions. In the x-direction, there should be no force (and thus no acceleration) acting on the ion k. Therefore, the motion of the ion k in the x-direction can be explained by the ion incident angle in the x-direction, the ion k's velocity in the z-direction, and the travel time at each section. The ion k's displacement in the x-direction at each section is given by

$$\Delta x_c = l_c \tan(\alpha_x) \tag{4a}$$

$$\Delta x_f = l_f \tan(\alpha_x) \tag{4b}$$

$$\Delta x_d = l_d \tan(\alpha_x) \tag{4c}$$

In the y-direction, depending on the ion k's velocity in the z-direction, the ion k may experience the resultant force that deflects the ion k in the y-direction. The ion k's displacement in the y-direction at each section is given by

$$\Delta y_c = l_c \tan(\alpha_y) \tag{5a}$$

$$\Delta y_f = l_f \tan(\alpha_y) + \frac{1}{2}\frac{q_k}{m_k}\frac{l_f^2}{v_{ion}^2}\left[E_y + v_{ion}B_x\right] \tag{5b}$$

$$\Delta y_d = l_d \tan(\alpha_y) + \frac{q_k}{m_k}\frac{l_f l_d}{v_{ion}^2}\left[E_y + v_{ion}B_x\right] \tag{5c}$$

In the collimator section, no E- and B-fields exist (Assumption 6)), and the motion of the ion k in the y-direction is given by the similar way of Eq. 4a.

The transmittancy of the three-section ExB probe is given by

$$T_k = \frac{S}{min(A_1, A_2, A_3, A_4)} = \frac{S}{A_1} \tag{6}$$

Unfortunately, there is no single formula that gives the intersection area of four circles from the given positions and sizes of the four circles circle. A step-by-step process to calculate the intersection area is described in Appendix A.

2. Ion current collection model

An ExB probe obtains the ExB probe spectrum by filtering out ions that do not have the Wien velocity. The ion current collected by the ExB probe at one electrode potential V_{plates} can be expressed as

$$I_{c,k}\big|_{V=V_{plates}} = A_1 q_k n_k \int_{v_w-\Delta v_w}^{v_w+\Delta v_w} \left[T_k\big|_{v_w=\frac{V_{plates}}{B_x d_e}}\, v f_k\right] dv \tag{7}$$

Since the transmittancy should be zero when the ion velocity is outside of the allowed velocity range ($v_w \pm \Delta v_w$), the integral in Eq. (7) can be expressed in the form of the matrix multiplication as

$$I_{c,k}\big|_{V=V_{plates}} = A_1 q_k n_k\, \boldsymbol{T_k}\big|_{v_w=\frac{V_{plates}}{B_x d_e}}\, v_{ion}\boldsymbol{f_k} \tag{8}$$

Here, $\boldsymbol{T_k}\big|_{v_w=\frac{V_{plates}}{B_x d_e}}$ is the $(1 \times N)$ array and $\boldsymbol{f_k}$ is the $(N \times 1)$ array. The collected ion current can also be represented as

$$I_{c,k}\big|_{V=V_{plates}} = A_1 q_k n_k v_w\, \boldsymbol{g_k}\big|_{v_w=\frac{V_{plates}}{B_x d_e}} \tag{9}$$

Comparing Eqs. (8) and (9), the ExB probe spectrum is obtained by

$$\boldsymbol{g_k} = \frac{v_{ion}}{v_w}\boldsymbol{T_k}\boldsymbol{f_k} \tag{10}$$

Here, $\boldsymbol{g_k}$ is the $(M \times 1)$ array, and $\boldsymbol{T_k}$ is the $(M \times N)$ matrix.

As shown in Sec. III.B.1, the transmittancy is a function of the ion incident angle as well. Therefore, the ExB probe spectrum should be given by

$$\begin{aligned}\boldsymbol{g_k} &= h(\alpha_{x,1},\alpha_{y,1})\frac{v_{ion}}{v_w}\boldsymbol{T_k}(\alpha_{x,1},\alpha_{y,1})\boldsymbol{f_k} + h(\alpha_{x,1},\alpha_{y,2})\frac{v_{ion}}{v_w}\boldsymbol{T_k}(\alpha_{x,1},\alpha_{y,2})\boldsymbol{f_k} + \ldots \\ &= \frac{v_{ion}}{v_w}\left[h(\alpha_{x,1},\alpha_{y,1})\boldsymbol{T_k}(\alpha_{x,1},\alpha_{y,1}) + h(\alpha_{x,1},\alpha_{y,1})\boldsymbol{T_k}(\alpha_{x,1},\alpha_{y,1}) + \ldots\right]\boldsymbol{f_k} \\ &= \frac{v_{ion}}{v_w}\sum_{i=1,j=1}^{N_{\alpha_x},N_{\alpha_y}}\left[h(\alpha_{x,i},\alpha_{y,j})\boldsymbol{T_k}(\alpha_{x,i},\alpha_{y,j})\right]\boldsymbol{f_k} = \frac{v_{ion}}{v_w}\overline{\boldsymbol{T}}_k\boldsymbol{f_k}\end{aligned} \tag{11}$$

When the distribution of the ion incident angle probability is uniform within the range from $-\alpha_{max}$ to $+\alpha_{max}$, $\overline{\boldsymbol{T}}_k$ can be obtained by averaging $\boldsymbol{T}_k\left(\alpha_x,\alpha_y\right)$ over the range from $-\alpha_{max}$ to $+\alpha_{max}$. The maximum possible ion incident angle in the y-direction, α_{max}, can be determined either from the ExB probe geometry or from the incoming ion beam properties.

C. Field non-uniformity effect

In Sec. III.B.1, we assumed that the E- and B-fields uniformly spanned the filtering region (Assumption 5)). However, simulations of the E- and B-fields in the ExB probe show that the E- and B-fields are not uniform and not identical in shape. Typical E- and B-field profiles in an ExB probe simulated by the ANSYS Maxwell simulation are shown in Fig. 3.

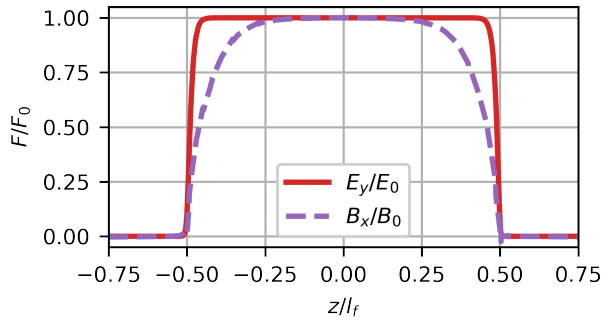

Fig. 3 Typical E- and B-field profiles along the z-direction in an ExB probe, simulated with ANSYS Maxwell. The field is normalized with a field strength at z = 0 mm (either E_0 or B_0) and the length of the filter region (l_f). The E- and B-fields are negligible in the collimator and the drift tube.

In the filter section, the acceleration in the y-direction due to the E- and B-fields is given by

$$a_{y,f}(z) = \frac{q_k}{m_k}\left[E_y(z) + v_{ion}B_x(z)\right] \tag{12}$$

Since the ion velocity in the z-direction remains unchanged (Assumption 6) in Sec. III.B.1), the velocity of the ion in the y-direction is given by

$$\begin{aligned}v_{y,f}(z) &= \int_0^t a_{y,f}(z')dt' + v_{y,0} \\ &= \int_0^z \left[\frac{q_k}{m_k}\left[E_y(z') + v_{ion}B_x(z')\right]\right]\frac{dz'}{v_{ion}} + v_{y,0} \\ &= \frac{q_k}{m_k}\frac{1}{v_{ion}}\int_0^z \left[E_y(z') + v_{ion}B_x(z')\right]dz' + v_{y,0}\end{aligned} \tag{13}$$

Over the filter region, the change in the ion velocity in the y-direction, which is the ion deflection in velocity, is given by

$$\begin{aligned}\Delta v_{y,f} &= v_{y,f}\big|_{z=l_f} - v_{y,0} \\ &= \frac{q_k}{m_k}\frac{1}{v_{ion}}\int_0^{l_f}\left[E_y(z') + v_{ion}B_x(z')\right]dz'\end{aligned} \tag{14}$$

Similarly, the position of the ion in the y-direction is given by

$$\begin{aligned}y_f(z) &= \int_0^t v_{y,f}(z')dt' + y_0 \\ &= \int_0^z \left[\frac{q_k}{m_k}\frac{1}{v_{ion}}\int_0^{z'}\left[E_y(s) + v_{ion}B_x(s)\right]ds + v_{y,0}\right]\frac{dz'}{v_{ion}} + y_0 \\ &= \frac{q_k}{m_k}\frac{1}{v_{ion}^2}\int_0^z\left[\int_0^{z'}\left[E_y(s) + v_{ion}B_x(s)\right]ds\right]dz' + \int_0^z\frac{v_{y,0}}{v_{ion}}dz' + y_0\end{aligned} \tag{15}$$

s is a dummy variable for the double integral of z'. The change in the ion position in the y-direction over the filter region is given by

$$\begin{aligned}\Delta y_f &= y_f\big|_{z=l_f} - y_0 \\ &= \frac{q_k}{m_k}\frac{1}{v_{ion}^2}\int_0^{l_f}\left[\int_0^{z'}\left[E_y(s) + v_{ion}B_x(s)\right]ds\right]dz' + \frac{v_{y,0}}{v_{ion}}l_f \\ &= \frac{q_k}{m_k}\frac{1}{v_{ion}^2}\int_0^{l_f}\left[\int_0^{z'}\left[E_y(s) + v_{ion}B_x(s)\right]ds\right]dz' + l_f\tan\left(\alpha_y\right)\end{aligned} \tag{16}$$

Eqs. (14) and (16) are the integral form of the ion deflection at the filter section due to the E- and B-fields that are not uniform.

It is desirable to make Eqs. (14) and (16) more convenient summation forms. In fact, it is difficult to express the E- and B-fields as a function of z, and the E- and B-field shapes are often obtained by a finite element numerical method such as FEMM [31] or ANSYS Maxwell. For any arbitrary field shapes, when the field is uniformly discretized into a small section with a width of δz, the acceleration due to the discretized E- and B-fields at the i-th section is given by

$$a_{y,f,i} = \frac{q_k}{m_k}\left[E_{y,i} + v_{ion}B_{x,i}\right] \tag{17}$$

By plugging Eq. (17) into Eq. (13), Eq. (14) can be expressed as

$$\begin{aligned}\Delta v_{y,f} &= \int_0^{l_f} a_{y,f}(z')\frac{dz'}{v_{ion}} \\ &= \sum_{i=0}^{N_s}\int_0^{\delta z} a_{y,f,i}\frac{dz'}{v_{ion}} \\ &= \frac{q_k}{m_k}\frac{1}{v_{ion}}\sum_{i=0}^{N_s}\int_0^{\delta z}\left[E_{y,i} + v_{ion}B_{x,i}\right]dz' \\ &= \frac{q_k}{m_k}\frac{1}{v_{ion}}\sum_{i=0}^{N_s}\left[E_{y,i} + v_{ion}B_{x,i}\right]\delta z \\ &= \frac{q_k}{m_k}\frac{l_f}{v_{ion}}\sum_{i=0}^{N_s}\left[E_{y,i} + v_{ion}B_{x,i}\right]\end{aligned} \tag{18}$$

Similarly, by plugging Eq. (17) into Eq. (13), Eq. (14) can be expressed as

$$\begin{aligned}
\Delta\tilde{y}_f &= \int_0^{l_f} v_y(z')\frac{dz'}{v_{ion}} \\
&= \sum_{i=0}^{N_s}\int_0^{\delta z} v_{y,f,i}(z')\frac{dz'}{v_{ion}} \\
&= \sum_{i=0}^{N_s}\int_0^{\delta z}\left[\int_0^{z'} a_{y,i}(s)\frac{ds}{v_{ion}} + v_{y,0}\right]\frac{dz'}{v_{ion}} \\
&= \frac{q_k}{m_k}\frac{1}{v_{ion}^2}\sum_{i=0}^{N_s}\int_0^{\delta z}\left[\int_0^{z'}\left[E_{y,i} + v_{ion}B_{x,i}\right]ds\right]dz' + \sum_{i=0}^{N_s}\int_0^{\delta z}\frac{v_{y,0}}{v_{ion}}dz' \\
&= \frac{q_k}{m_k}\frac{1}{v_{ion}^2}\sum_{i=0}^{N_s}\int_0^{\delta z}\left[\left[E_{y,i} + v_{ion}B_{x,i}\right]z'\right]dz' + \frac{v_{y,0}}{v_{ion}}\sum_{i=0}^{N_s}\int_0^{\delta z}dz' \\
&= \frac{q_k}{m_k}\frac{1}{v_{ion}^2}\sum_{i=0}^{N_s}\left[E_{y,i} + v_{ion}B_{x,i}\right]\frac{\delta z^2}{2} + \frac{v_{y,0}}{v_{ion}}\sum_{i=0}^{N_s}\delta z \\
&= \frac{1}{2}\frac{q_k}{m_k}\frac{l_f^2}{v_{ion}^2}\sum_{i=0}^{N_s}\left[E_{y,i} + v_{ion}B_{x,i}\right] + l_f\tan\left(\alpha_y\right). \qquad (19)
\end{aligned}$$

Eqs. (18) and (19) are useful because the ion deflection can be estimated for any field geometry as long as they satisfy the Riemann integrability. Even though we assume that no E- and B-fields are present in the drift tube, the y-displacement in the drift tube section is affected by the field non-uniformity. The y-displacement in the drift tube is given by

$$\begin{aligned}
\Delta\tilde{y}_d &= \int_0^{l_d} v_y(z')\frac{dz'}{v_{ion}} \\
&= \int_0^{l_d}\left[\Delta v_{y,f} + v_{y,0}\right]\frac{dz'}{v_{ion}} \\
&= \left[\frac{q_k}{m_k}\frac{l_f}{v_{ion}}\sum_{i=0}^{N_s}\left[E_{y,i} + v_{ion}B_{x,i}\right] + v_{y,0}\right]\frac{l_d}{v_{ion}} \\
&= \frac{q_k}{m_k}\frac{l_f l_d}{v_{ion}^2}\sum_{i=0}^{N_s}\left[E_{y,i} + v_{ion}B_{x,i}\right] + l_d\tan\left(\alpha_y\right). \qquad (20)
\end{aligned}$$

Eqs. 19 and 20 indicate that the area under the curve of the E- and B-fields must be known. The effective E- and B-field strengths are given by

$$E_{y,\text{eff}} = \int_0^{l_f} E_y(z)dz \approx \sum_{i=0}^{N_s} E_{y,i} \qquad (21)$$

$$B_{x,\text{eff}} = \int_0^{l_f} B_x(z)dz \approx \sum_{i=0}^{N_s} B_{x,i} \qquad (22)$$

Since the E-field strength at the center of the filter region typically matches with the theory (Eq. 2, $E_{y,0} = V_{plates}/d_e$), it is convenient to keep the E-field as it is. Instead, we introduce the practical B-field strength that is given by

$$B_{x,\text{pra}} = B_{x,0}\frac{B_{x,\text{eff}}/B_{x,0}}{E_{y,\text{eff}}/E_{y,0}} = B_{x,\text{eff}}\frac{E_{y,0}}{E_{y,\text{eff}}} \qquad (23)$$

Therefore, when the E- and B-fields are not uniform and not identical in shape, the y-displacements in the filter

section and the drift tube section should be given by

$$\Delta\tilde{y_f} = l_f \tan(\alpha_{in}) + \frac{1}{2}\frac{q_k}{m_k}\frac{l_f^2}{v_{ion}^2}\left[E_{y,0} + v_{ion}B_{x,\text{pra}}\right] \tag{24}$$

$$\Delta\tilde{y_d} = l_d \tan(\alpha_{in}) + \frac{q_k}{m_k}\frac{l_f l_d}{v_{ion}^2}\left[E_{y,0} + v_{ion}B_{x,\text{pra}}\right] \tag{25}$$

Eqs. 24 and 25 replace Eqs. 5b and 5c when the E- and B-fields are not uniform. For the case $\alpha_y = 0$, the Wien velocity for the ExB fields that are not uniform and not identical in shape is given by

$$v_w^* = \frac{E_{y,\text{eff}}}{B_{x,\text{eff}}} = \frac{E_{y,0}}{B_{x,\text{pra}}} = \frac{V_{plates}}{B_{x,\text{pra}}d_e} \tag{26}$$

D. IVDF-based Ion Parameters

1. Signal strength level

The signal strength, or the peak height, should be large compared to the measurement noise level in order to observe all peaks in the measured I-V curve. The signal strength level can be estimated from the ion current density and the ExB probe geometry as

$$\begin{aligned} I_{peak,k} &= A_1 J_{tot}\frac{\bar{v}_k}{\sum_k^{N_p}(\%_k\bar{v}_k)}\max(\boldsymbol{g_k}) \\ &= A_1 J_{tot}\frac{\bar{v}_k}{\sum_k^{N_p}(\%_k\bar{v}_k)}\max\left(\frac{v_{ion}}{v_w}\boldsymbol{T_k}\boldsymbol{f_k}\right) \end{aligned} \tag{27}$$

As shown in Eq. (27), in order to estimate the peak height of the collected current, the relative ion species fraction and the IVDF have to be known. Therefore, to estimate the signal strength level before measurements, one must estimate the ion beam condition (the total current density, the relative ion species fraction, and the shape of IVDF).

2. Relative species fraction

The relative ion species fraction in number density can be obtained from the IVDF as

$$\%_{n,k} = \frac{n_k}{\sum_k^{N_p} n_k} = \frac{\int_0^\infty \boldsymbol{f_k}dv}{\sum_k^{N_k}\int_0^\infty \boldsymbol{f_k}dv} \tag{28}$$

When the measured ExB probe spectrum is close to the true IVDF ($\boldsymbol{g_k} \approx \boldsymbol{f_k}$), the relative ion fraction can be approximately obtained from their ExB probe spectra as

$$\%_{n,k} = \frac{n_k}{\sum_k^{N_p} n_k} = \frac{\int_0^\infty \boldsymbol{g_k}dv}{\sum_k^{N_k}\int_0^\infty \boldsymbol{g_k}dv}. \tag{29}$$

IV. Test 1: Single Ion Motion under Non-Uniform ExB Fields

A. Test 1 Setup

In this section, the derived analytical formulas that correct the E- and B-field non-uniformity (Eqs. 24 and 25) are tested against the numerical simulation of a single ion trajectory. Figure 3 shows the E- and B-field profiles along the z-axis simulated by ANSYS Maxwell. The grade of the permanent magnet is N42. The magnet is sandwiched by two 416 stainless steel plates to make the B-field more uniform in the filter region. The design of the ExB probe is described in Sec. IV.A, and Appendix C provides the ANSYS Maxwell simulation conditions to generate the plots in Fig. 3. Based on the ANSYS Maxwell simulation, the E- and B-fields at the center of the filter region ($E_{y,0}$ and $B_{x,0}$) are -9,999.72

V/m for V_{plates} = 100 V and 0.144 Tesla, respectively. The effective E- and B-field strengths ($E_{y,\text{eff}}$ and $B_{x,\text{eff}}$) are 9,743.90 V/m and 0.126 Tesla, respectively. The practical B-field strength ($B_{x,\text{pra}}$), given by Eq. (23), is therefore approximately 0.1294 Tesla.

In this work, we assume ions have a negligible velocity in the x-direction. The numerical domain is 2D in z-y coordinates, with a size of 152.4 mm × 10.0 mm and a cell array of 1525 × 101 (each cell size is in 0.1 mm × 0.1 mm square). The Ar^+ ion is assumed accelerated by a potential of 500 V (v_{ion} = 49145.43 m/s) and injected through the entrance at z = -76.2 mm and y = 0.0 mm. The initial ion velocity in the z- and y-direction is given by

$$v_{z,0} = v_{ion} \cos\left(\alpha_y\right) \approx v_{ion} \tag{30a}$$

$$v_{y,0} = v_{ion} \sin\left(\alpha_y\right) \tag{30b}$$

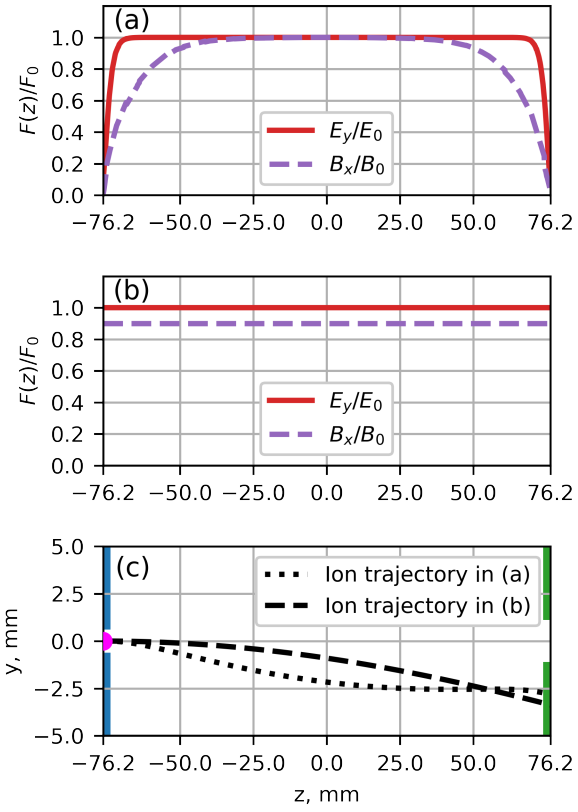

Fig. 4 (a) The non-uniform field profile normalized in magnitude. The solid red line shows the E-field profile, and the dashed purple line shows the B-field profile. (b) The uniform field profile normalized in magnitude with the practical B-field strength. The solid red line shows the E-field profile, and the dashed purple line shows the B-field profile. (c) The Ar^+ ion trajectory under the non-uniform fields. The z = -76.2 mm plane is the entrance, and the z = +76.2 mm plane is the exit of the filter region. The dimension is not scaled.

Figure 4(a) shows the E- and B-field profiles normalized in magnitude. We use the simulated E- and B-field profiles that are obtained by ANSYS Maxwell simulation (Fig. 3). To test Eqs. 24 and 25, the uniform E- and B-fields are defined with the practical B-field strength. Figure 4(b) shows the uniform E- and B-field profile normalized in magnitude. In Fig. 4(b), the B-field is normalized with $B_{x,0}$ of 0.144 Tesla. The Boris-Bunemannn Lorentz force integration scheme is implemented to push the particle. The local field strength is linearly interpolated within each cell based on the particle position. The velocity and position evaluation is conducted with a leap-frog method, and a half-timed pushback for initial velocity is performed at the beginning of the simulation. The time step size is 10^{-9} s, at least 100 times shorter than the ion cyclotron timescale in the tested condition. The result does not change significantly for the time step size

that is smaller than 10^{-9} s. The particle push is repeated until the calculated ion position is located at either z > 76.2 mm, y > 5.0 mm, or y < -5.0 mm. When the particle push is stopped, the ion velocity and position are re-calculated by linearly interpolating them at the final and penultimate time steps. Figure 4(c) shows the ion trajectory under the ExB fields that are shown in Fig. 4(a) and (b). In the case of Fig. 4, the E-field strength at the center of the filter section (E_0) is chosen to be -1.05$v_{ion}B_0$ ≈ -6672.94 V/m. The Ar^+ ion is deflected in the negative y-direction since the force due to the E-field is higher than the one from the B-field by 5%. We set α_{in} = 0° in this test.

B. Test 1 Result

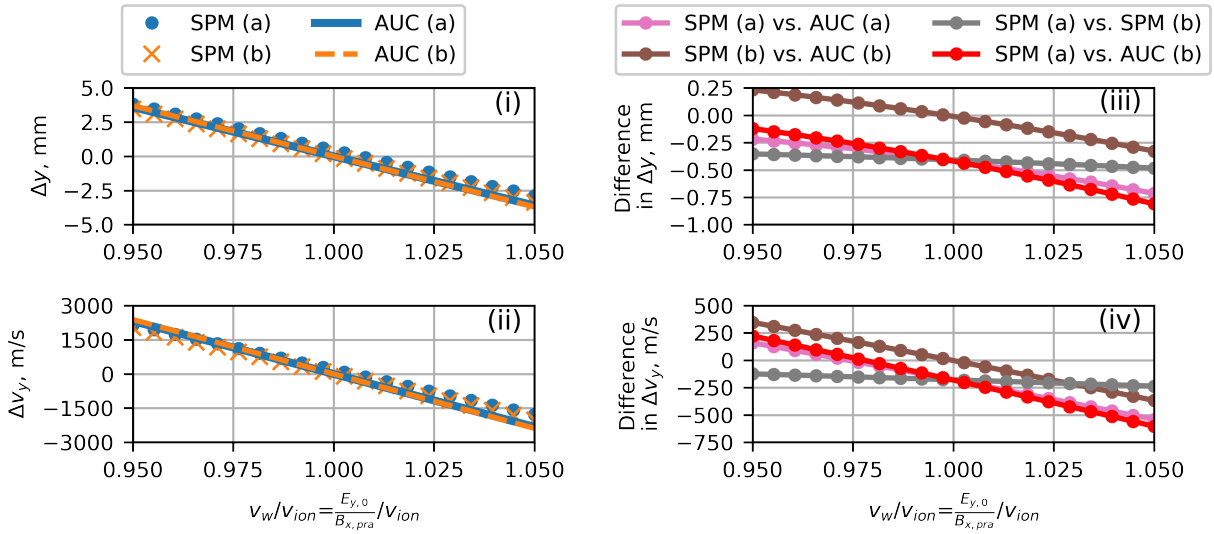

Fig. 5 Comparison of the simulated (SPM = Single Particle Motion) and calculated (AUC = Area Under the Curve) ion deflections in the y-direction. (i) Simulated and calculated changes in the ion y-position under the non-uniform fields (Fig. 4(a)) and the uniform fields (Fig. 4(b)). (ii) Simulated and calculated changes in the ion velocity under the non-uniform fields (Fig. 4(a)) and the uniform fields (Fig. 4(b)). (iii) Difference in the simulated and calculated changes in the ion y-position shown in Fig. 5(i)). (iv) Difference in the simulated and calculated changes in the ion y-velocity shown in Fig. 5(ii)).

Figure 5(i) and (ii) shows the simulated (SPM = Single Particle Motion) and calculated (AUC = Area Under the Curve) ion deflections under the non-uniform fields (Fig. 4(a)) and the uniform fields (Fig. 4(b)). Figure 5(i) shows the change in the ion position in the y-direction, and Figure 5(ii) shows the change in the ion velocity in the y-direction. The uniform E-field strength varied from 0.95$v_{ion}B_0$ to 1.05$v_{ion}B_0$. Each dot represents the condition of the numerical simulation tests where 20 different E_0 were tested in this numerical experiment case. Figure 5(iii) and (iv) shows the difference of the deflections obtained by different techniques and assumptions. The pink and brown lines in Fig. 5(iii) and (iv) compare two techniques of calculating the ion deflections under the non-uniform and uniform fields. These two techniques have calculated the changes in the y-displacement with an error of ±0.75 mm and the changes in the y-velocity with an error of ± 750 m/s. These results have validated their accuracy against each other. The gray lines in Fig. 5(iii) and (iv) compare the ion deflection under the non-uniform fields and under the uniform fields using the single particle motion code. The approximation of the non-uniform fields to the uniform fields using $B_{x,\text{pra}}$ still captures the ion deflection with an error of -0.5 mm or less for Δy and -500 m/s or less for Δv_y. Finally, the red lines compares the simulated ion deflection under the non-uniform field and the calculated ion deflections under the uniform field with $B_{x,\text{pra}}$. The analytical formula using $B_{x,\text{pra}}$ captures the ion deflection under the non-uniform fields with an error of -1 mm (approximately 30% percentage difference) or less for Δy and with an error of -750 m/s (approximately 33% percentage difference) or less for Δv_y. Note that the percentage difference error goes to infinity because the denominator decreases to zero as the ratio of velocity v_w/v_{ion} approaches to the center (one).

V. Test 2: ExB Probe Spectra from Test IVDF

A. Test 2 Setup

1. Test IVDF: Ar^+-N_2^+-N^+ ion beam

For the test 2, we consider an ion beam of a mixture of Ar^+-N_2^+-N^+ ions with a 1:1:1 number density ratio. For simplicity, we assume that the density of other ions, such as Ar^{2+}, is negligible. The IVDF for ion k in the beam is modeled with a Gaussian distribution function, which is given by

$$f_k(v) = F_k \exp\left[-\left(\frac{v-\mu_k}{\sqrt{2}\sigma_k}\right)^2\right] \tag{31}$$

In this work, we assume the acceleration potential of 250 V, and the peak velocity for ion k is given by Eq. (1) and the peak width is 5% of the peak velocity ($\sigma_k = 0.05\mu_k$). The ratio of the highest peak amplitudes (Ar^+ in this work) to one of the other ion species k is given by

$$\frac{F_{Ar^+}}{F_k} = \frac{\frac{1}{\sqrt{2\pi}\sigma_{Ar^+}}}{\frac{1}{\sqrt{2\pi}\sigma_k}} = \sqrt{\frac{m_k}{m_{Ar^+}}} \tag{32}$$

The total test IVDF is a super-position of individual IVDF, and it is given by

$$f(v) = f_{Ar^+}(v) + f_{N_2^+}(v) + f_{N^+}(v) \tag{33}$$

We model our ion beam source as a cluster of point sources, and each point source emits a conical ion beam with a divergence angle (θ_{div}) of 5°. We consider the source to have a diameter of 10 cm, and our ExB probe is placed 1 m away. The ExB probe x-y plane and the ion source plane are parallel to each other. With a 5° beam divergence angle, the diameter of the ion beam is approximately 8.75 cm at 1 m away ($\approx 1\text{ m} * \tan(\theta_{div})$), and we, therefore, assume that the ion enters the ExB probe with an incident angle that is within ±5° of a uniform distribution. We assume that the beam divergence from the point source is independent of the mass-to-charge ratio.

2. ExB probe designs

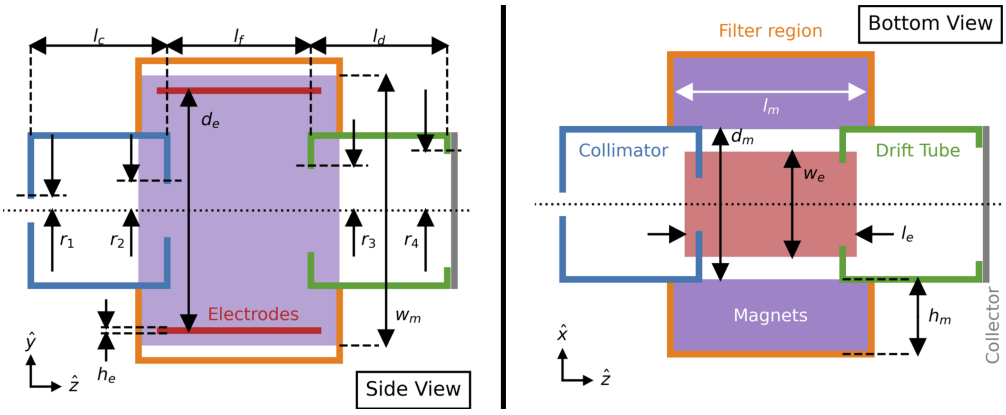

Fig. 6 ExB diagram in the yz-plane and the xz-plane. Not scaled.

Figure 6 shows the geometry of the ExB probe used in this work. The ExB probe is made of three sections: a collimator, a filter region, and a drift tube. Table 1 summarizes three designs of the ExB probe tested in this work. The geometric parameters used in Design 1 and Design 2 are the same. Design 1 utilizes the field non-uniformity correction and uses the practical B-field. Design 2 assumes the uniform E- and B-fields and uses the B-field strength at the center of the filter section.

The angular-averaged transmittancy matrix is obtained by Eq. (11) with a uniformly distributed α_x and α_y. Figure 7 shows the angular-averaged transmittancy matrix for Ar^+, N_2^+, and N^+ ions for the ExB probe Design 1. Figure

Table 1 The design parameters of the ExB probe.

Parameter	Design 1	Design 2	Design 3	Unit
r_1	4.0	4.0	4.0	mm
r_2	4.0	4.0	4.0	mm
r_3	4.0	4.0	4.0	mm
r_4	4.0	4.0	4.0	mm
l_c	135.0	135.0	65.0	mm
l_f	152.4	152.4	152.4	mm
l_d	135.0	135.0	65.0	mm
B_x	0.129	0.144	0.129	Tesla

8 shows the angular-averaged transmittancy matrix for Ar^+ ion for the ExB probe Design 1, 2, and 3. Since T_k is approximately zero at $\alpha_x \geq |1.5|^\circ$, we set $\alpha_{x,max} = 1.5^\circ$ with $N_{\alpha_x} = 7$. For the y-direction, we use the ion source's beam divergence assumption and set $\alpha_{y,max} = 5^\circ$ with $N_{\alpha_y} = 41$. Since some of the α are larger than the collimator's maximum allowance ion incident angle ($= \tan^{-1}((r_1 + r_2)/l_c)$) and such a α makes the transmittancy to be zero, the transmittancy levels in Figs. 7 and 8 do no reach one even when v_{ion} is equal to v_w. Appendix B summarizes the transmittancy matrix at different α_x and α_y.

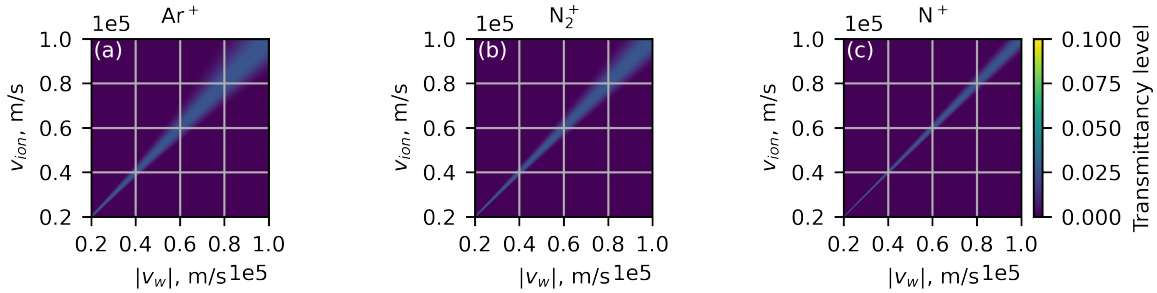

Fig. 7 The angular-averaged transmittancy matrix $\overline{T}_k$: (a) Ar^+, (b) N_2^+, and (c) N^+. The design is Design 1.

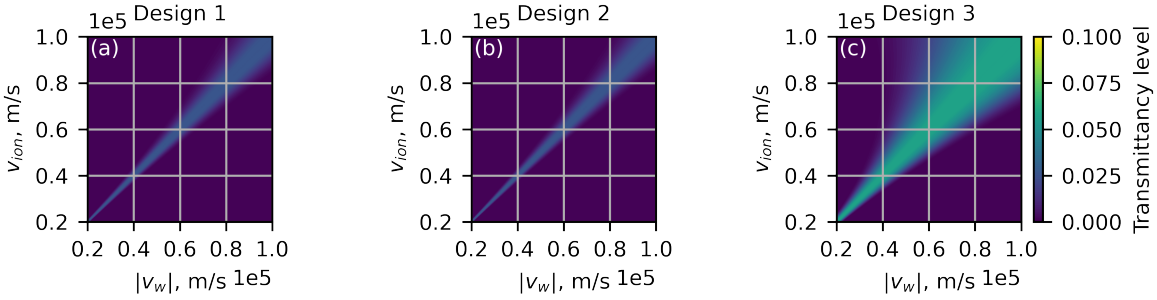

Fig. 8 The angular-averaged transmittancy matrix $\overline{T}_k$: (a) Design 1, (b) Design 2, and (c) Design 3. k = Ar^+.

B. Test 2 Results

Figure 9 shows the test IVDF defined in Sec. V.A and the ExB probe spectra from different ExB probe designs. Both the IVDF and the ExB probe spectra is normalized so that the highest peak is equal to one. The shapes of the ExB probe spectra from Design 1 and 2 ExB probes are similar because they share the same geometric parameters. However, since Design 2 overestimates the B-field strength, it underestimates the ion velocity (Eq. 2: $v_w = E_y/B_x$). Unlike those two, Design 3 ExB probe fails to capture the true IVDF. Design 3 ExB probe broadens all three peaks and makes two distinct, closely adjacent peaks (Ar^+ and N_2^+) into one large peak. In this work, we can obtain the ion-specific parameters (i.e., the peak velocity, the FWHM, etc.) from the ion-specific ExB probe spectrum that is calculated with Eq. 10. However, during the actual ExB probe operation, the first task after collecting the ExB probe spectrum is applying the curve-fit and decomposing it into the ion-specific ExB probe spectra. Even though we can assume the number of peaks in the ExB probe spectrum (i.e., the number of ion species in the ion beam), it is difficult to decompose the measured ExB probe spectrum into the ion-specific ExB probe spectrum from the green line in Fig. 9 with a low uncertainty.

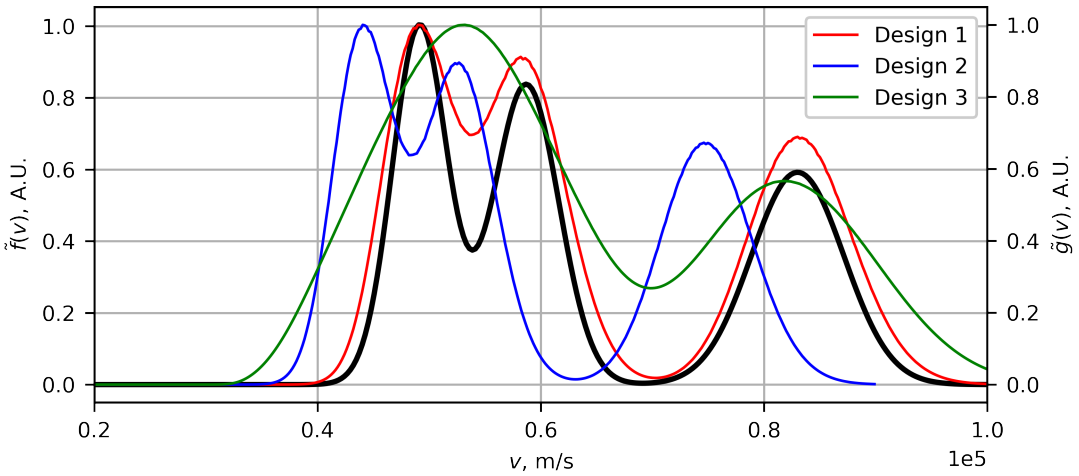

Fig. 9 Test IVDF (black line) and ExB probe spectra (colored lines).

Table 2 Ion-based parameters from the test IVDF and from the ExB probe spectra for three designs. The value in the parenthesis represents the percentage difference with respect to the test IVDF value. Since no data available for $I_{peak,k}/J_{tot}$ for the test IVDF, no percentage differences are shown for $I_{peak,k}/J_{tot}$.

Parameter	Ion	Test IVDF	Design 1	Design 2	Design 3
μ_k, m/s	Ar^+	49145.43	49000.00 (-0.3%)	44044.94 (-10.38%)	47400.00 (-3.55%)
	N_2^+	58687.79	58600.00 (-0.15%)	52674.16 (-10.25%)	57400.00 (-2.19%)
	N^+	82997.06	83000.00 (-0.00%)	74606.74 (-10.11%)	81800.00 (-1.44%)
FWHM$_k$, m/s	Ar^+	5790.41	7616.68 (31.54%)	7253.36 (25.27%)	16637.90 (187.34%)
	N_2^+	6910.62	8463.53 (22.47%)	8169.83 (18.22%)	16933.67 (145.04%)
	N^+	9771.31	10845.37 (10.99%)	10653.73 (9.03%)	17064.05 (74.63%)
$I_{peak,k}/J_{tot}$, - (No data available for Test IVDF)	Ar^+	-	2.83e-6	2.66e-6	8.46e-6
	N_2^+	-	1.16e-6	1.08e-6	3.77e-6
	N^+	-	5.08e-7	4.65e-7	1.97e-6
$\%_{n,k}$, %	Ar^+	33.33	33.35 (0.06%)	33.35 (0.06%)	33.62 (0.87%)
	N_2^+	33.33	33.34 (0.03%)	33.33 (0.00%)	33.47 (0.42%)
	N^+	33.33	33.31 (-0.06%)	33.31 (-0.06%)	32.92 (-1.23%)

Table 2 summarizes the ion parameters from the test IVDF and the calculated ExB probe spectra. Note that the ion parameters are obtained from the calculated ion-specific ExB probe spectrum and no curve-fit is performed in this work. The value in the parenthesis represents the percentage difference with respect to the test IVDF value. Since no data available for $I_{peak,k}/J_{tot}$ for the test IVDF, no percentage differences are shown for $I_{peak,k}/J_{tot}$.

Design 1 ExB probe captures the peak ion velocities with an error of 100 m/s or less. As mentioned above, Design 2 ExB probe underestimates the peak ion velocity by the overestimation of the B-field strength. Design 3 ExB probe slightly underestimates the peak ion velocities with an error of 2000 m/s or less. However, these values are obtained from the ion-specific ExB probe spectra; the one large peak that contains both Ar^+ and N_2^+ peaks needs to be decomposed in order to obtain the ion peak velocities during the actual ExB probe operation. Note that the acceleration potential can be estimated from the N^+ peak velocity ($V_{accel} \approx \frac{1}{2}(\frac{m_{N^+}}{q_{N^+}})\mu_{N^+}^2 \approx 554.78$ V), and the peak velocities of Ar^+ and N_2^+ can be estimated from it (Eq. 1: $\mu_{Ar^+} \approx 51767.55$ m/s and $\mu_{N_2^+} \approx 57841.33$ m/s). Since the peak shift in the ExB probe spectra is dependent on the ion species, the above estimation does not match well with the peak velocities in the test IVDF nor the peak velocities from the ion-specific ExB probe spectra.

For the peak width, all ExB probe designs broaden the peak width. Design 3 ExB probe broadens the peak width the most; the calculated peak width for Ar^+ is approximately 2.87 times larger than the actual peak width. In this numerical experiment test, this broadening is too large compared to the difference between the peak velocities, and it made two peaks into one large peak.

The third row of Tab. 2 shows the signal strength level given by Eq. 27, which is the peak current strength with respect to the total ion beam current density. Since Eq.27 is a function of the ExB probe spectrum, no data available for the test IVDF and we leave the columns as blank. Design 3 ExB probe provides the highest signal strength compared to other two designs. The signal strengths from Design 3 ExB probe are at least three times higher than other signal strengths from other two designs. The peak current strength must be high enough compared to the background noise in the measurement system in order to resolve the ExB probe spectra. Design 3 ExB probe gives the worst performance in terms of capturing the ExB probe shape, but it will provides the lowest signal-to-noise ratio.

Although there are differences in the true (test) IVDF and the measured (calculated) ExB probe spectra, the relative ion species fractions from the ExB probe spectra calculated with Eq. 29 show a good agreement with an error of 0.1% or less. The ExB probe gives rise to difference in the IVDF and the ExB probe spectrum for all ions. Based on the transmittancy concept discussed in Sec. III.B.1, the mechanism to cause the difference in the IVDF and the ExB probe spectrum is species-dependent, and it can be observed in the difference in the $\bar{\boldsymbol{T}}_k$ matrix for different ions (Fig. 7). However, in this numerical experiment, the ions have similar mass-to-charge ratios, and therefore, the relative sizes of the area under the curve still remained.

VI. Space-Charge Ion Beam Expansion Analysis

We have assumed that the ion beam does not diverge or converge in the ExB probe (Assumption 2)). However, depending on the power level of the EP thruster or the location of the ExB probe, the ion current density may be high enough to cause the non-negligible space-charge and the beam expansion in the ExB probe. The expansion of the ion beam due to the space-charge effect after passing the orifice [32] can be expressed as

$$\frac{r(z)}{r_o} = 1 + 2.6866 \times 10^{10} \frac{z^2}{v_k^3} \frac{q_k}{m_k} \frac{I_k}{\pi r_o^2} \tag{34}$$

Figure 10 shows the ion beam expansion rate due to the space-charge effect given by Eq. 34. The orifice radius is set to 4.0 mm. The solid lines represent the case when the ion is Ar^+, and the dotted line shows the case when the ion is Xe^+. In this work, the ion current I_k is calculated by the current density times the orifice area ($I_k = J_k \cdot \pi r_o^2$). Three ion current densities, 20 A/m^2 (blue), 0.2 A/m^2 (orange), and 2 mA/m^2 (green) are tested. 20 A/m^2 is the Xe^+ ion current density from the BHT-200 HET at the nominal operating condition measured at approximately 30 cm away [33]. We consider that the ExB probe will not be placed near the EP thruster because the ExB probe may perturb the thruster operation due to its size and the leaking B-field. We assume that 20 A/m^2 is the maximum current density that an ExB probe will encounter. Note that the ion current I_k in Eq. 34 is assumed to be the ion current due to the ion having an uniform velocity v_k [32]. Since the ion beam from the EP thruster typically has an IVDF, the ion current I_k in Eq. 34 may be smaller than the ion current calculated from the EP thruster current density. Therefore, ion beam expansion rates for smaller current density at 0.2 A/m^2 and 2 mA/m^2 are also tested.

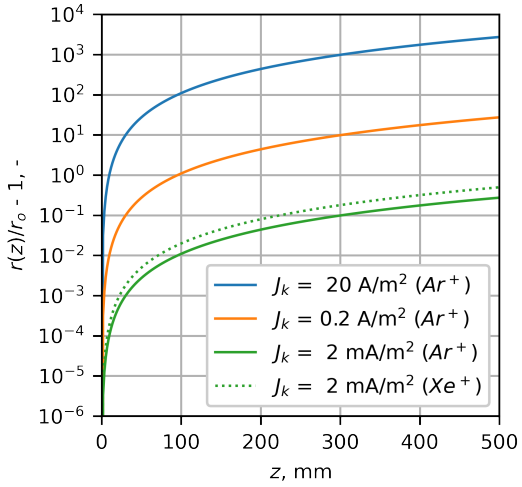

(a) v_k is calculated by Eq. 1 with V_{accel} = 500 V. At z = 0, the beam expansion rate is 1, and so the line goes to zero in this log-scale plot.

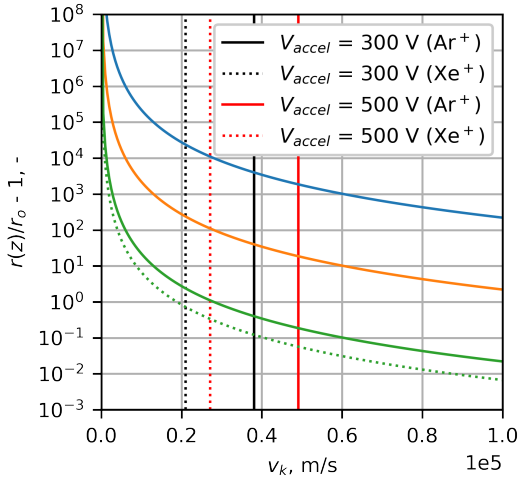

(b) z = 412.4 mm = $l_c + l_f + l_d$ (Design 1 and 2). Black vertical line show the ion velocities at V_{accel} = 300 V, and red vertical lines the ion velocity at V_{accel} = 500 V.

Fig. 10 The ion beam expansion rate due to the space-charge effect given by Eq. 34 for various I_k. r_o = 4.0 mm.

Figure 10a shows the ion beam expansion rate vs. the distance from the orifice. The ion velocities are calculated by Eq. 1 with V_{accel} = 500 V. When the acceleration potential is fixed, the ion beam expansion rate is larger for the heavier ions because the ion beam expansion rate is proportional to $\sqrt{m_k}\,(\frac{r(z)}{r_o} - 1 \propto \frac{1}{v_k^3 m_k} \propto \frac{1}{1/m_k^{3/2}} \frac{1}{m_k} \propto m_k^{1/2})$. The ion beam expansion rate significantly changes with the ion current density. For 20 A/m^2, the ion beam radius becomes 100 times larger at z = 100 mm. However, the ion beam expansion rate is approximately 2 for 0.2 A/m^2 at z = 100 mm, and it is approximately 1 (no expansion) for 2 mA/m^2 at z = 100 mm. The space-charge effect expands the ion beam with a distance, and so keeping the ExB probe short is one of the approaches to minimize the beam expansion effect.

Figure 10b shows the ion beam expansion rate vs. the ion velocity at the z = 412.4 mm. Blue, orange, and green lines represents the ion beam expansion rates for different ion current density same as the one in Fig. 10a. The black vertical lines represent the ion velocities at V_{accel} = 300 V, and the red vertical lines represent the ion velocities at V_{accel} = 500 V. In Fig. 10b, the ion beam expansion rate is larger for the lighter ions because the velocity is not dependent on the ion species in Fig. 10b, and the ion beam expansion rate is proportional to $1/m_k$ $(r(z)/r_o - 1 \propto \frac{1}{m_k})$. As shown in Fig. 10a, the ion beam expansion rate is highly dependent on the ion current level. The ion beam expansion rate is also highly dependent on the velocity and it becomes larger at a lower velocity. In the Test IVDF in Sec. V, the population of the ion velocity lower than 0.4×10^5 m/s is very small, and the space-charge beam expansion effect for the low velocity ions can be ignored in the transmmittancy analysis.

VII. Conclusion

In this work, the difference in the ExB probe spectrum and the IVDF was examined. The ion beam trajectory in the ExB probe was analyzed, and the ion current collection was modeled with an effective ion collection area. The E- and B-field non-uniformity was included in the analysis, and the analytical correction formula was proposed and tested. The ExB probe spectra were calculated from three different ExB probe designs to study how ExB probe design affects the difference in the IVDF and the ExB probe spectrum. Finally, the ion beam expansion due to the space-charge effect in the ExB probe is analyzed.

In the numerical experiment test 1, we compared the motion of the single ion particle under the given E- and B-fields. The non-uniform fields were defined based on the actual field profiles simulated by the ANSYS Maxwell, and the practical B-field strength that accounts for the field non-uniformity was calculated. The changes in the ion position and velocity in the y-direction over the filter section were calculated by the simulation of the single ion particle motion and by the analytical formula based on the field strength and the equation of motions. The analytical formula with $B_{x,\mathrm{pra}}$

captures the ion deflection under the non-uniform fields; the error sizes (-1 mm or less for Δy and -750 m/s or less for Δv_y) are comparable to the error sizes of other comparison (e.g., the simulation and the calculation for the non-uniform fields case), and it can be concluded that the analytical formula proposed in this work can be used to account for the field non-uniformity effect.

In the numerical experiment test 2, we compared the ExB probe spectra calculated from three different ExB probe designs by Eq. 10 and compared them to the synthetically defined test IVDF. Design 1 ExB probe captures the peak velocities very well with an error of 0.3% or less. Since Design 2 ExB probe overestimates the B-field strength, it underestimates the ion velocity by approximately 10%. Even though Design 1 ExB probe capture the peak velocity, it still broadens the peak width at least 11%. Therefore, inferring the ion velocity spread from the measured ExB probe spectra may not be the valid approach. Design 3 ExB probe broadens the peak width the most (up to +187%) and makes two distinct, closely adjacent peaks into one large peak. Although Design 3 ExB probe provides the worst IVDF capturing performance out of three designs, it provides at least three times higher signal strength and thus provides at least three times lower signal-to-noise ratios among the designs tested in this work. Therefore, when designing the ExB probe, one must balance the IVDF capturing performances and the signal strength levels. All ExB probe designs tested in this work captures the relative ion species fraction very well with an error of 1.5% or less.

The ion beam expansion due to the space-charge effect is analyzed. It is found that keeping the ExB probe short is one of the approaches to minimize the beam expansion effect. The ion beam expansion rate increases by $\frac{1}{v_k}$, and so it is important to evaluate it using the full velocity range in the IVDF. It is found that the space-charge beam expansion is highly dependent on the ion current level; the ion beam expansion rate decreases from 100 to 1 when the ion current density drops from 20 A/m^2 to 2 mA/m^2. Therefore, another approach to minimize the beam expansion effect is to limit the ion current into the ExB probe; this can be achieved by placing the ExB probe further away from the EP thruster. When designing the ExB probe and considering the operating condition, one must consider the space-charge effect to make sure the beam expansion is small enough in the ExB probe. After testing and validating the model of the ion beam expansion such as the one suggested by Li [32], the ion beam expansion can be included in the ExB probe spectrum analysis.

Appendix A: Intersection Area of Four Circles

This section summarizes the step-by-step process to calculate the intersection area of four aperture circles in this work. First, we calculate the ion beam displacements in the x- and y-directions at each section using Eqs. 4 and 5. For the displacements in the y-direction at the filter section and the drift tube section, Eqs. 24 and 24 should be used instead of Eqs. 5b and 5c if E- and B-fields shape is known from the simulation or the measurement. Note that the center of each circle can be obtained by

$$(x_1, y_1) = (0, 0) \tag{35a}$$

$$(x_2, y_2) = (x_1 + \Delta x_c, y_1 + \Delta y_c) \tag{35b}$$

$$(x_3, y_3) = (x_2 + \Delta x_f, y_2 + \Delta y_f) \tag{35c}$$

$$(x_4, y_4) = (x_3 + \Delta x_d, y_3 + \Delta y_d) \tag{35d}$$

The distance between the centers of two circles i and j is given by

$$\Delta r_{i,j} = \sqrt{(\Delta x_{i,j})^2 + (\Delta y_{i,j})^2} \tag{36}$$

When any of two circle pair satisfies "$(r_i + r_j)^2 \leq (\Delta r_{i,j})^2$", these two circles do not overlap and thus the intersection area is zero. Then, we output $S = 0$ m^2 and terminate the calculation. When all of two circle pair satisfies "$(r_i - r_j)^2 \geq (\Delta r_{i,j})^2$", all circles are completely overlapped each other. Then, we output $S = min(A_1, A_2, A_3, A_4)$ ($=A_1$ by Assumption 9)) and terminate the calculation. Figure 11 summarizes the process up to this point. The process in Fig. 11 determines if the intersection area calculation must be performed or not and saves the calculation time.

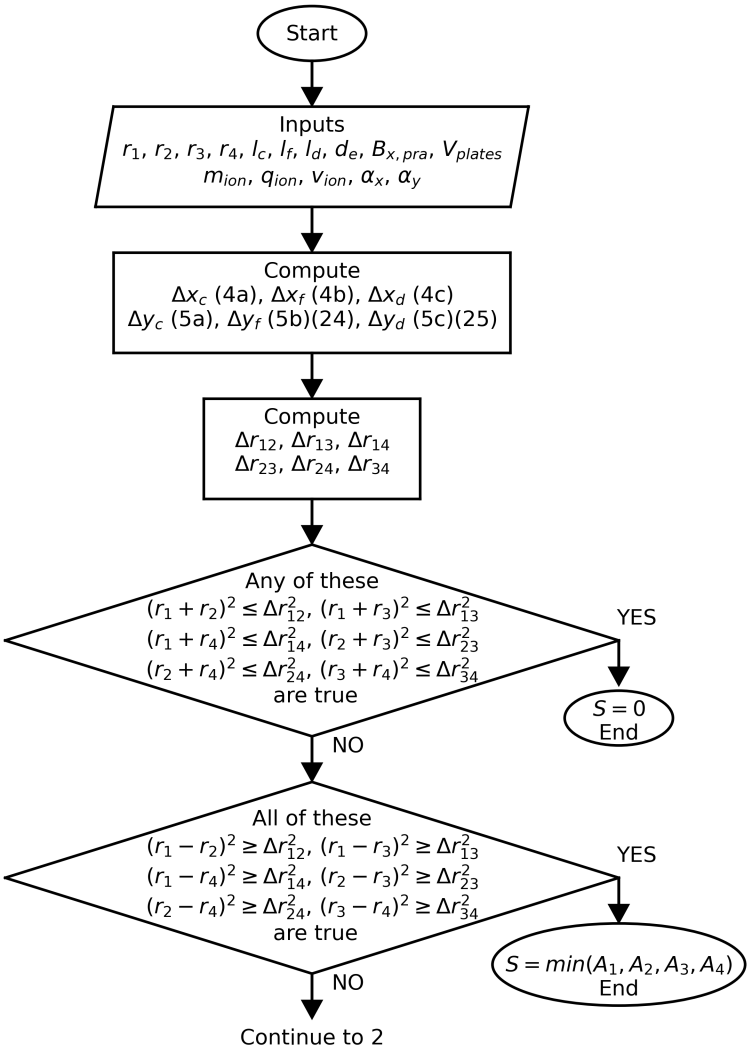

Fig. 11 The first half of the flow chart for the intersection area of four circles. This part determines if the intersection area is zero or A_1 based on the sizes and positions of four circles.

Now we know the intersection area is smaller than at least one aperture circle area. The way of calculating the intersection area is different based on the number of circles overlapping and making the intersection area. In order to know how many and which circles make the intersection area, the location of the intersecting points are calculated. For four circles, there are six pairs of two circles (e.g., 1 and 2, 2 and 3, etc.) and there are at most 12 or less intersection points. The intersection points that makes the intersection area has to be within all four circles. The number of the intersection points is equal to the number of circles that makes the intersection area. Figure 12 summarizes the process of determining the shape of the intersection area (i.e., the number of the circles that make the intersection area).

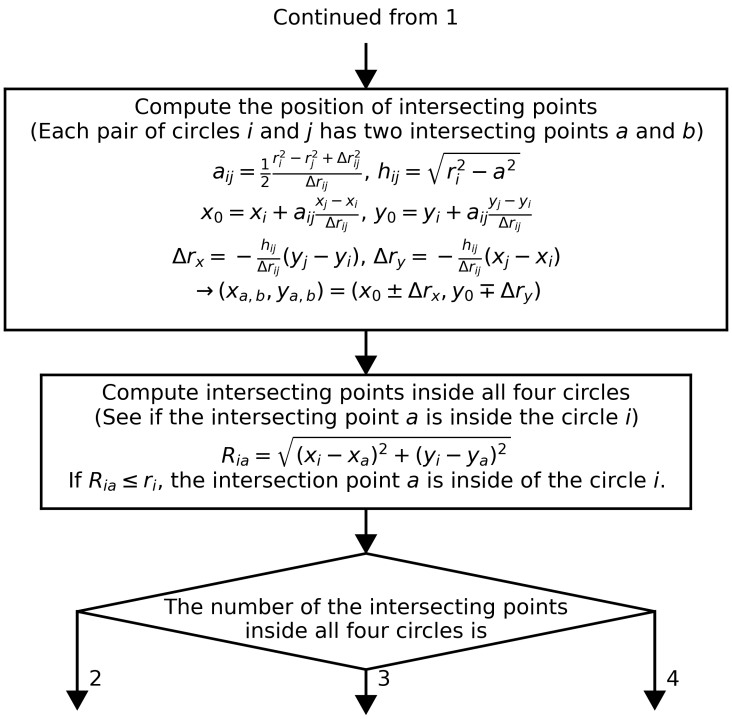

Fig. 12 The second half of the flow chart for the intersection area of four circles. This part determines which circle makes the intersection area.

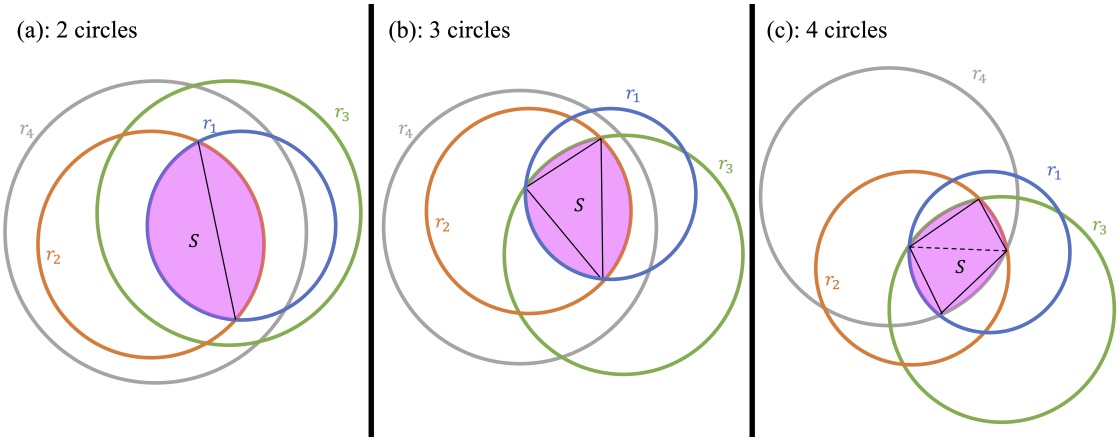

Fig. 13 Three types of the intersection area of four circles based on the number of circles that makes the intersection area. (a) Two circles, (b) Three circles, and (c) Four circles.

Figure 13 shows three types of the intersection area shape based on the number of circles that make the intersection

area. When two circles make the intersection area, the intersection area is given by

$$S = r_i^2 \tan^{-1}\left(\frac{\sqrt{4r_i^2\Delta y_{ij}^2 - \left(r_i^2 - r_j^2 + \Delta y_{ij}^2\right)^2}}{r_i^2 - r_j^2 + \Delta y_{ij}^2}\right) + r_j^2 \tan^{-1}\left(\frac{\sqrt{4r_j^2\Delta y_{ij}^2 - \left(r_j^2 - r_i^2 + \Delta y_{ij}^2\right)^2}}{r_j^2 - r_i^2 + \Delta y_{ij}^2}\right) - \frac{1}{2}\sqrt{4r_i^2\Delta y_{ij}^2 - \left(r_i^2 - r_j^2 + \Delta y_{ij}^2\right)^2} \quad (37)$$

When three circles make the intersection area, the intersection area can be obtained by summing the arc areas and the central triangle(s). The area of the central triangle(s) can be obtained with Heron's formula. The area of the arcs can be obtained by subtracting the triangle area from the sector area.

Appendix B: Transmittancy matrix at different α_x and α_y

Figure 14 shows the transmittancy matrix for different incident angles. The transmittancy is largest when $\alpha_x = \alpha_y = 0°$. The incident angle in the y-direction alters the shape of the transmittancy matrix because the change in the ion position in the y-direction due to the incident angle can be cancelled by the force due to the E- and B-fields. On the other hands, the incident angle in the x-direction reduces the level in the transmittancy matrix while keeping the shape. Since there is no force in the x-direction, the ion with a finite incident angle in the x-direction may be filtered out and does not contribute to the ion current collection. This result indicates that the assumption of neglecting the incident angle in the x-direction may be useful for speeding up the calculation while maintaining the quality of the analysis.

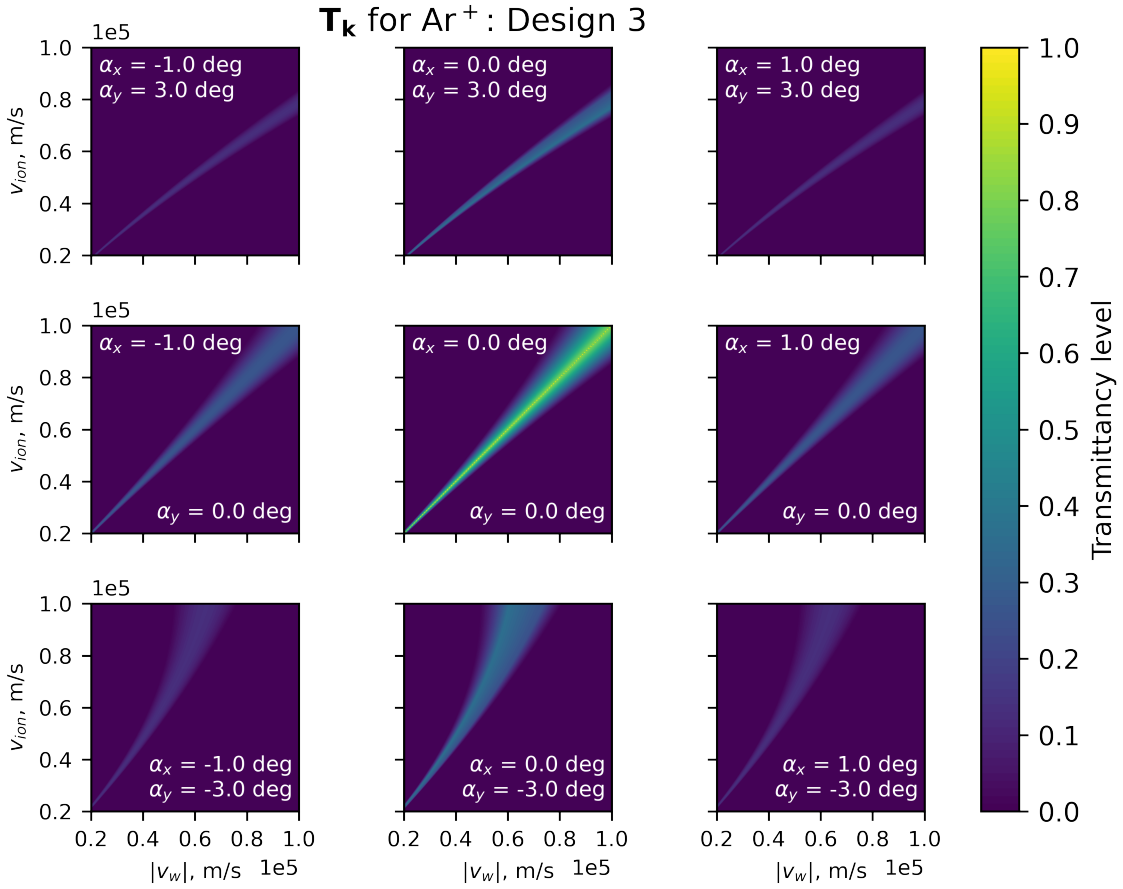

Fig. 14 Transmittancy matrix for different incident angles in the x- and y-directions. The ion is Ar^+ and the ExB probe design is Design 3.

Appendix C: ANSYS Maxwell simulation conditions

The E- and B-fields in the ExB probe were calculated with an ANSYS® Maxwell, Release 2022 R2. The permanent magnet used in the ExB probe is a neodymium magnet and the grade is N42. The N42 magnet is defined with a Relative Permeability of 1.05, a Bulk Conductivity of 625,000 Siemens/m, Magnetic Coercivity Magnitude of 995,000 A/m. The 416 stainless steel is used to sandwich the N42 magnet to generate a more uniform B-field in the ExB probe. The 416 stainless steel is magnetic, and the B-H curve characteristic is taken from the material library in the FEMM [31]. Table 3 summarizes the ExB probe's geometric parameters required for the E- and B-field simulation.

Table 3 The geometric parameters of the ExB probe for the E- and B-fields simulation. Units are in mm. The dimensions for the magnets include two 416 stainless steel plates per magnet.

Parameter	Symbol	Value
Electrode separation distance	d_e	10.0
Electrode length	l_e	157.48
Electrode width	w_e	35.56
Electrode height	h_e	2.0
Magnet separation distance	d_m	38.1
Magnet length	l_m	152.4
Magnet width	w_m	76.2
Magnet height	h_m	50.8

Acknowledgments

This work is supported by the Air Force Office of Scientific Research through Grant AF FA9550-23-1-0025 (Dr. Mitat Birkan as the program monitor).

References

[1] Vahrenkamp, R., "Measurement of double charged ions in the beam of a 30-cm mercury bombardment thruster," *10th Electric Propulsion Conference*, American Institute of Aeronautics and Astronautics, Lake Tahoe,NV,U.S.A., 1973. https://doi.org/10.2514/6.1973-1057, URL https://arc.aiaa.org/doi/10.2514/6.1973-1057.

[2] Kuang, Y.-Z., Shen, G.-Q., and Yang, S.-T., "ExB momentum analyses for broad-beam ion sources," *19th International Electric Propulsion Conference*, American Institute of Aeronautics and Astronautics, Colorado Springs,CO,U.S.A., 1987. https://doi.org/10.2514/6.1987-1081, URL https://arc.aiaa.org/doi/10.2514/6.1987-1081.

[3] Takegahara, H., Kasai, Y., Gotoh, Y., Miyazaki, K., Hayakawa, Y., Kitamura, S., Nagano, H., and Nanamura, K., "Beam characteristics evaluation of ETS-VI Xenon ion thruster," *IEPC paper*, Seattle, Washington, 1993, pp. 93–235.

[4] Williams, G. J., Jr., Domonkos, M. T., and Chavez, J. M., "Measurement of Doubly Charged Ions in Ion Thruster Plumes," *27th International Electric Propulsion Conference*, Pasadena, CA, 2001.

[5] Kim, S.-W., and Gallimore, A. D., "Plume Study of a 1.35-kW SPT-100 Using an ExB Probe," *Journal of Spacecraft and Rockets*, Vol. 39, No. 6, 2002, pp. 904–909. https://doi.org/10.2514/2.3897, URL https://arc.aiaa.org/doi/10.2514/2.3897.

[6] Kim, S.-W., "Experimental investigations of plasma parameters and species-dependent ion energy distribution in the plasma exhaust plume of a Hall thruster," Ph.D. thesis, University of Michigan, 1999.

[7] Hofer, R., and Gallimore, A., "Ion species fractions in the far-field plume of a high-specific impulse Hall thruster," *39th AIAA/ASME/SAE/ASEE Joint Propulsion Conference and Exhibit*, American Institute of Aeronautics and Astronautics, Huntsville, Alabama, 2003. https://doi.org/10.2514/6.2003-5001, URL https://arc.aiaa.org/doi/10.2514/6.2003-5001.

[8] Beal, B. E., "CLUSTERING OF HALL EFFECT THRUSTERS FOR HIGH-POWER ELECTRIC PROPULSION APPLICATIONS," Ph.D. thesis, University of Michigan, 2004.

[9] Ekholm, J., and Hargus, W., "E x B Measurements of a 200 W Xenon Hall Thruster," *41st AIAA/ASME/SAE/ASEE Joint Propulsion Conference & Exhibit*, American Institute of Aeronautics and Astronautics, Tucson, Arizona, 2005. https://doi.org/10.2514/6.2005-4405, URL http://arc.aiaa.org/doi/abs/10.2514/6.2005-4405.

[10] Reid, B., Shastry, R., Gallimore, A., and Hofer, R., "Angularly-Resolved ExB Probe Spectra in the Plume of a 6-kW Hall Thruster," *44th AIAA/ASME/SAE/ASEE Joint Propulsion Conference & Exhibit*, American Institute of Aeronautics and Astronautics, Hartford, CT, 2008. https://doi.org/10.2514/6.2008-5287, URL http://arc.aiaa.org/doi/abs/10.2514/6.2008-5287.

[11] Brown, D. L., "INVESTIGATION OF LOW DISCHARGE VOLTAGE HALL THRUSTER CHARACTERISTICS AND EVALUATION OF LOSS MECHANISMS," Ph.D. thesis, University of Michigan, 2009.

[12] Shastry, R., Hofer, R., Reid, B., and Gallimore, A., "Method for Analyzing ExB Probe Spectra from Hall Thruster Plumes," *44th AIAA/ASME/SAE/ASEE Joint Propulsion Conference & Exhibit*, American Institute of Aeronautics and Astronautics, Hartford, CT, 2008. https://doi.org/10.2514/6.2008-4647, URL http://arc.aiaa.org/doi/abs/10.2514/6.2008-4647.

[13] Huang, W., Shastry, R., Soulas, G. C., and Kamhawi, a. H., "Farfield Plume Measurement and Analysis on the NASA-300M and NASA-300MS," *33th International Electric Propulsion Conference*, Washington, DC, 2013.

[14] Lim, Y., Kim, H., Choe, W., Lee, S. H., Seon, J., and Lee, H. J., "Observation of a high-energy tail in ion energy distribution in the cylindrical Hall thruster plasma," *Physics of Plasmas*, Vol. 21, No. 10, 2014, p. 103502. https://doi.org/10.1063/1.4897178, URL https://pubs.aip.org/aip/pop/article/376475.

[15] Kim, H., Lim, Y., Choe, W., and Seon, J., "Effect of multiply charged ions on the performance and beam characteristics in annular and cylindrical type Hall thruster plasmas," *Applied Physics Letters*, Vol. 105, No. 14, 2014, p. 144104. https://doi.org/10.1063/1.4897948, URL http://aip.scitation.org/doi/10.1063/1.4897948.

[16] Huang, W., and Shastry, R., "Analysis of Wien filter spectra from Hall thruster plumes," *Review of Scientific Instruments*, Vol. 86, No. 7, 2015, p. 073502. https://doi.org/10.1063/1.4923282, URL http://aip.scitation.org/doi/10.1063/1.4923282.

[17] Wang, X., Xu, Z., Wang, P., Huang, Y., and Cui, G., "Experimental and numerical studies of low power Hall thruster performance," *Journal of Innovation and Development*, Vol. 2, No. 3, 2023, pp. 133–139. https://doi.org/10.54097/jid.v2i3.7550, URL https://drpress.org/ojs/index.php/jid/article/view/7550.

[18] Homann, K. H., and Traube, J., "Use of a Wien Filter for Mass and Velocity Analysis of Charged Soot Particles in a Nozzle Beam," *Berichte der Bunsengesellschaft für physikalische Chemie*, Vol. 91, No. 8, 1987, pp. 828–833. https://doi.org/10.1002/bbpc.19870910814, URL https://onlinelibrary.wiley.com/doi/10.1002/bbpc.19870910814.

[19] Anderson, J., and Fitzgerald, D., "Fullerene propellant research for electric propulsion," *32nd Joint Propulsion Conference and Exhibit*, American Institute of Aeronautics and Astronautics, Lake Buena Vista,FL,U.S.A., 1996. https://doi.org/10.2514/6.1996-3211, URL https://arc.aiaa.org/doi/10.2514/6.1996-3211.

[20] Nakayama, Y., and Takegahara, H., "C60 Application to Ion Thruster-Inspection of Ionized and Extracted Particle," *25th International Electric Propulsion Conference*, Cleveland, OH, 1997.

[21] Snyder, J. S., "Investigation of the Feasibility of Fullerene Propellant for Ion Thrusters," Ph.D. thesis, Colorado State University, Nov. 1998.

[22] Koda, D., and Hitoshi, K., "Measurements of Ion Beam Accelerated from a Fullerene Negative Ion Thruster," *H27 Uchu Yusou Symposium*, 2016.

[23] Koda, D., "Laboratory Experiment on Negative Ion Propulsion using Fullerene C60," Ph.D. thesis, The University of Tokyo, Mar. 2017.

[24] Gerst, D., Renaud, D., Mazouffre, S., Chabert, P., and Aanesland, A., "ExB probe investigation of the PEGASES thruster ion beam in Xe and SF6," *IEPC Paper*, Washington D.C., USA, 2013.

[25] Gerst, J. D., "Investigation of magnetized radio frequency plasma sources for electric space propulsion," Ph.D. thesis, UNIVERSITÉ D'ORLÉANS, Nov. 2013.

[26] Renaud, D., Mazouffre, S., and Aanesland, A., "Plasma composition and ion acceleration in the PEGASES thruster." *Space Propulsion Conference*, Cologne, Germany, 2014.

[27] Renaud, D., Gerst, D., Mazouffre, S., and Aanesland, A., "E × B probe measurements in molecular and electronegative plasmas," *Review of Scientific Instruments*, Vol. 86, No. 12, 2015, p. 123507. https://doi.org/10.1063/1.4937604, URL http://aip.scitation.org/doi/10.1063/1.4937604.

[28] Gurciullo, A., Fabris, A. L., and Cappelli, M. A., "Ion plume investigation of a Hall effect thruster operating with Xe/N2 and Xe/air mixtures," *Journal of Physics D: Applied Physics*, Vol. 52, No. 46, 2019, p. 464003. https://doi.org/10.1088/1361-6463/ab36c5, URL https://iopscience.iop.org/article/10.1088/1361-6463/ab36c5.

[29] Gurciullo, A., "Electric propulsion technologies for enabling the use of molecular propellants," Ph.D. thesis, University of Surrey, Nov. 2020.

[30] Hofer, R. R., "Development and Characterization of High-Efficiency, High-Specific Impulse Xenon Hall Thrusters," Ph.D. thesis, University of Michigan, 2004.

[31] Meeker, D. C., "Finite Element Method Magnetics," , ???? URL https://www.femm.info.

[32] Li, G., Duan, Y., and Hieftje, G. M., "Space-charge Effects and Ion Distribution in Plasma Source Mass Spectrometry," *Journal of Mass Spectrometry*, Vol. 30, No. 6, 1995, pp. 841–848. https://doi.org/10.1002/jms.1190300609, URL https://onlinelibrary.wiley.com/doi/10.1002/jms.1190300609.

[33] Nakles, M., Brieda, L., Reed, G., Hargus, W., and Spicer, R., "Experimental and Numerical Examination of the BHT-200 Hall Thruster Plume," *43rd AIAA/ASME/SAE/ASEE Joint Propulsion Conference & Exhibit*, American Institute of Aeronautics and Astronautics, Cincinnati, OH, 2007. https://doi.org/10.2514/6.2007-5305, URL http://arc.aiaa.org/doi/abs/10.2514/6.2007-5305.